ACS APPLIED NANO MATERIALS

Article

Pulsed Laser Deposition and Characterization of Hetero-epitaxial LiMnO/LaSrCoO3 Bilayer Thin Films as Model Lithium Ion Battery Cathodes

Xiankai Yu, Xiao Chen, D. Bruce Buchholz, Scott A. Barnett, Qianqian Li, Jinsong Wu, Paul Fenter, Michael J. Bedzyk, and Vinayak P. Dravid

ACS Appl. Nano Mater., **Just Accepted Manuscript** • DOI: 10.1021/acsanm.7b00133 • Publication Date (Web): 02 Jan 2018

ACS Publications

ACS Applied Nano Materials is published by the American Chemical Society. 1155 Sixteenth Street N.W., Washington, DC 20036

Pulsed Laser Deposition and Characterization of Hetero-epitaxial $LiMn_2O_4/La_{0.5}Sr_{0.5}CoO_3$ Bilayer Thin Films as Model Lithium Ion Battery Cathodes

Xiankai Yu,[†] Xiao Chen,[†] D. Bruce Buchholz,[†] Scott A. Barnett,[,†] Qianqian Li,[‡] Jinsong Wu,[‡] Paul A. Fenter,[¶] Michael J. Bedzyk,[†] Vinayak P. Dravid[‡]*

†Department of Materials Science and Engineering, Northwestern University, Evanston, IL 60208, USA

‡NUANCE, Northwestern University, Evanston, IL 60208, USA

¶Chemical Sciences and Engineering Division, Argonne National Laboratory, 9700 South Cass Avenue, Argonne, IL 60439, United States

KEYWORDS: $LiMn_2O_4$, hetero-epitaxial thin film, conductive buffer layer, characterization, interface, crystal structure, lithium ion battery.

ABSTRACT: Epitaxial $LiMn_2O_4$ (LMO) – $La_{0.5}Sr_{0.5}CoO_3$ (LSCO) bi-layer thin films were grown on single crystalline $SrTiO_3$ (STO) (111) substrates as model lithium ion battery

cathodes. The LSCO layer was used as an electrically conducting buffer layer for electrochemical testing. The LMO and LSCO layers were both epitaxial, with sub-nano flat LMO/LSCO interfaces as seen by X-ray diffraction, synchrotron X-ray scattering, and high-resolution transmission electron microscopy (HRTEM), but with a large LMO surface roughness due to the relatively large lattice mismatch with LSCO. 3D islands and depressions were formed on the strain-relaxed LMO layer and misfit dislocations at the LMO/LSCO interface were discerned through HRTEM imaging, suggesting a Stranski-Krastanov (SK) mode thin film growth. A crystalline structural change from cubic spinel at the LMO surface and interior to tetragonal oxygen-deficient LMO at the LMO/LSCO interface was examined. Electrochemical tests along with *in situ* synchrotron X-ray scattering measurements on the epitaxial LMO/LSCO bilayers showed a significant loss of capacity after the first cycle, which was attributed to an electrical conductivity loss of the LSCO buffer layer due to irreversible lattice oxygen loss.

1. INTRODUCTION

Lithium ion batteries (LIBs) are now widely used for sustainable transport, such as full electric vehicles (EVs) and hybrid electric vehicles (HEVs), and portable devices such as laptops and mobile phones, due to their high energy and power densities.[1,2] Lithium manganese oxide $LiMn_2O_4$ (LMO) is a well-established LIB cathode material with the characteristics of low cost, low toxicity, good structural and chemical stability, a good Mn^{3+}/Mn^{4+} redox potential (4.1 V vs. Li/Li^+), and fast charging rates.[3–5] Despite these merits, one critical obstacle for LMO-based LIBs is its loss of capacity upon repeated electrochemical cycling, especially at elevated temperature.[6,7] LMO capacity fading is

attributed to Mn^{2+} dissolution into the electrolyte through a disproportionation reaction, detrimental electrolyte decomposition resulting in the formation of a solid electrolyte interface (SEI) layer, irreversible interphase formation, and cooperative Jahn-Teller distortion of $Mn^{3+}O_6$ octahedra (high spin $3d^4$, $t_{2g}^3e_g^1$) at a deep state of discharge.[8–10] These reactions remain poorly understood and accurate characterizations are limited due to the complex interface between LMO and the liquid electrolyte. For instance, many factors including surface morphology, surface impurity, surface reconstruction, crystal defects and grain boundaries significantly affect the (electro)chemical reactions at a polycrystalline LMO/electrolyte interface. Besides, complicated kinetics exist at the electrode surface, including electron transport between the current collector and electrode, lithium ion intercalation and extraction at the interface, and lithium ion diffusion within the electrodes.[11]

Advanced *in situ* characterization at the molecular level is important for precisely examining the interfacial reaction processes. Epitaxially grown LMO thin films are ideal for such fundamental studies[12–19]. When well prepared, they can provide well-defined LMO surfaces with low defect densities, well-defined crystallographic orientation, and a small lattice strain. Unlike particle-based electrodes, the thin film geometry is well suited for interface study by a range of advanced *in situ* and *ex situ* characterization tools such as X-ray photoelectron spectroscopy (XPS), synchrotron X-ray scattering and absorption spectroscopy, atomic force microscopy (AFM), and high-resolution scanning transmission electron microscopy (STEM).[20–24] Epitaxial films grown on different orientation substrates allow one to probe interfacial effects on different-orientation LMO surfaces; for example, it would be possible to check DFT calculations indicating that the LMO (111) surface is more resistant to Mn dissolution than other orientations.[25,26]

To date, epitaxial LMO thin films have been successfully grown on various substrates, such as $SrTiO_3$, MgO, Al_2O_3, Pt and Au, using a variety of deposition techniques including pulsed laser deposition (PLD), radio-frequency (r.f.) magnetron sputtering, atomic layer deposition (ALD) and chemical solution deposition (CSD).[18,24,27–32] Most ceramic oxide substrates and LMO thin films have relatively poor electrical conductivity. Thus, to carry out electrochemical tests on epitaxial LMO films, a conducting back contact to the LMO electrode is required. Nb-doped $SrTiO_3$ (STO) substrates (0.5% Nb) are one option, providing a useful conductivity of $5x10^{-3}$ Ω cm at ambient temperature.[8,18] However, Nb-doped STO can lose conductivity at oxidizing conditions, either during LMO film growth (typically with a background O_2 pressure), or upon electrochemical cycling at the elevated potentials associated with delithiation of cathode materials. Alternatively, $SrRuO_3$, Pt, and Au have been grown as conductive back-contact buffer layers prior to the growth of LMO thin films.[1,24,28,33,36,37] It is well known that noble metals like Pt and Au have poor wettability with oxide substrates, making them unsuitable for uniform epitaxial oxide film growth, especially at high temperature which is required to get LMO of high crystallinity.[34]

Hirayama et al. were the first to examine interfacial structural change between liquid electrolytes and epitaxial LMO thin films grown on conductive Nb-doped STO substrates of different crystalline orientations using *in situ* and *ex situ* XRR and XRD measurements.[1,8,24] However, in situ observations of the interfacial reactions were extremely limited due to poor epitaxy and/or bad electrochemical reversibility of the LMO thin films. Gao et al. used EELS-STEM to analyze local LMO compositions and structure gradients as a function of the distance from the interface of epitaxial LMO thin films on Au.[36] So far, most current HRTEM studies have been focused on the interface between LMO and the substrate rather than the LMO/electrolyte interface. Therefore, model LMO thin films of high epitaxy and

electrochemical reversibility are desired for comprehensive characterizations of electrode/electrolyte interfaces by in situ X-ray scattering and HRTEM. The same approach is also important for studying other electrode materials, including LMO with transition metal doping or surface coating.[38-40]

In this study, we report the structure and electrochemical reactivity of hetero-epitaxial bilayers of LMO/LSCO grown on single crystal STO (111) substrates using pulsed laser deposition (PLD). The perovskite oxide LSCO was chosen as a conductive buffer layer based on its high metallic conductivity (~ 10^4 S/cm at room temperature) and its good lattice match with both STO (–1.7%) and spinel LMO (7.5%). The bilayer crystal structure, epitaxy and surface/interface roughnesses were observed by synchrotron X-ray diffraction, X-ray reflectivity, AFM, and high resolution TEM. The reversibility and stability of these bilayers were probed by electrochemical cycling and *in situ* synchrotron X-ray scattering.

2. EXPERIMENTAL DETAILS

Sample Preparation. A stoichiometric $LiMn_2O_4$ target (2 inch in diameter, MTI, 99.99% purity) was used as the PLD source material. The $La_{0.5}Sr_{0.5}CoO_3$ PLD target was prepared as follows. The LSCO powder was first synthesized using solid state reaction(42) from La_2O_3 (Sigma-Aldrich, ⩾ 99.9%), $SrCO_3$ (Sigma-Aldrich, ⩾ 99.9%) and $CoCO_3$ (Alfa Aesar, ⩾ 99.5%). These powders were mixed through a roller ball mill for 48 h, followed by firing at 1100 ^oC for 24 h in air. The heating rate was 120 ^oC/h while the cooling rate was kept at 90 ^oC/h. The resulting LSCO powder was then ball milled in ethanol for 72 h. The as-synthesized LSCO powder obtained X-ray diffraction peaks (upper line in **Figure 1**) that match well with standard $La_{0.5}Sr_{0.5}CoO_3$ (ICSD #184073), indicating successful synthesis of high-crystallinity LSCO powder. Bulk $La_{1-x}Sr_xCoO_3$ (x = 0.5) has a slightly rhombohedrally

distorted crystal structure with a pseudo cubic lattice constant a_c = 3.837 Å (inset in **Figure 1**); the calculated lattice constant a_c was 3.835 Å from the 110 reflection.[41,42] For PLD target fabrication, the prepared LSCO powder was first tape cast (Tape Casting Warehouse, INC.) onto a polyethylene (PET) carrier film. The tapes were then cut, stacked and hot laminated at 80 ^{o}C for 30 min under a pressure of 5000 psi. Finally, the laminated stack was punched into a pellet with 1.2-inch diameter, and sintered at 1350 ^{o}C for 24 h in air, yielding a 1-inch diameter 3 mm thick LSCO target with a density of around 90%.

The LMO and LSCO layers were grown on STO (111) substrates using a KrF excimer laser with a wavelength of 248 nm and a PLD apparatus (PLD/MBE 2300, PVD Products, Inc.). The substrates were acetone washed and pre-annealed at 1000 ^{o}C for 8 h in air. The LMO and LSCO deposition conditions are summarized in **Table 1**. Two bilayer thin films with different LSCO buffer layer thicknesses (5 nm and 10 nm) were grown in order to examine the effect of buffer layer thickness on the crystallographic perfection and surface morphology of LMO layer. After LSCO growth, PLD conditions were immediately switched for subsequent LMO growth. Avoiding air exposure between the two growth steps proved to be important, as initial experiments where the LSCO film were taken out of the vacuum chamber prior to LMO growth yielded films of poor quality. To get high electrical conductivity and good crystallinity of LSCO buffer layer, a large O_2 partial pressure (300 mTorr) and relatively high substrate temperature were applied.[43,44] Additionally, a slow cooling rate of 5 ^{o}C/min was chosen to avoid oxygen deficiency in LSCO buffer layers.[45,46] Both LMO and LSCO single layers were also synthesized on STO (111) substrates as controls.

Table 1. PLD conditions for epitaxial LMO/LSCO/STO (111) bilayer thin films.

Target	Temperature (°C)	Working distance (mm)	Duration time (s)	Laser fluence (mJ/pulse)	Frequency (Hz)	O_2 partial pressure (mTorr)
LMO	650	75	150	200	5	30
LSCO	650	60	260	270	5	300

Sample Characterization. Inductively Coupled Plasma Mass Spectrometry (ICP-MS, Thermo Scientific™ iCAP Q) was used to determine the Li:Mn and La:Sr:Co ratios in the films. The surface morphology and roughness of all thin films were observed by Atomic Force Microscopy (AFM, Bruker Dimension FastScan®). Powder X-ray diffraction was done on Scintag XDS2000 with Cu Kα (λ = 1.5406 Å) radiation. Epitaxy and crystal orientations were characterized by thin-film X-ray diffraction (ATX-G, Rigaku) with Cu Kα (λ = 1.5406 Å, incident slit = 0.2 mm) radiation. X-Ray reflectivity (ATX-G, Rigaku) measurements were conducted to calculate thickness and roughness of each layer by fitting the XRR data using a Motofit package in Igor Pro software (WaveMetric, INC.). Cross-sectional TEM samples of LMO/LSCO bilayers were prepared by a dual-beam focused ion beam (FIB, FEI Helios Nanolab 600) with a 1-μm-thick protective Pt layer on the sample surface. High resolution TEM (JEOL Co., JEM-2100F) observations were conducted at 200 kV with a field-emission gun electron source.

Electrochemical Test. Electrochemical measurements were performed using a specially designed spectroelectrochemical cell for *in operando* synchrotron X-ray scattering measurements in a "transmission" geometry.[47] The cells were assembled inside an argon

glove box with lithium metal as the counter/reference electrodes, the LMO/LSCO bilayer thin films as the working electrode and 1:1 EC/DMC + 1 M $LiPF_6$ as the electrolyte. Cyclic voltammetry (CV) scans were performed using a Potentiostat/Galvanostat (CHI760d, INC) electrochemical analyzer. The potential was swept from 2.5 V to 4.3 V at intervals of 0.5 mV/s. *In situ* synchrotron X-ray scattering measurements were performed during the cycling process at Advanced Photon Source (APS) sector 33BM-C in Argonne National Laboratory (ANL), using a four-circle Huber diffractometer and a Pilatus 100k area detector with X-ray photon energy of 20.000 keV (λ = 0.6198 Å) and an incident flux of ~10^{10} photons/s. The X-ray beam (with cross section of 2 × 0.2 mm^2 and divergence of 40 μrad = 0.0005 $Å^{-1}$ along 2θ direction) illuminated a 2 mm × 3 mm area on the sample.

3. RESULTS AND DISCUSSION

Growth results for LSCO and LMO single layers on STO substrates are described first, followed by a discussion of results for LMO/LSCO bi-layers.

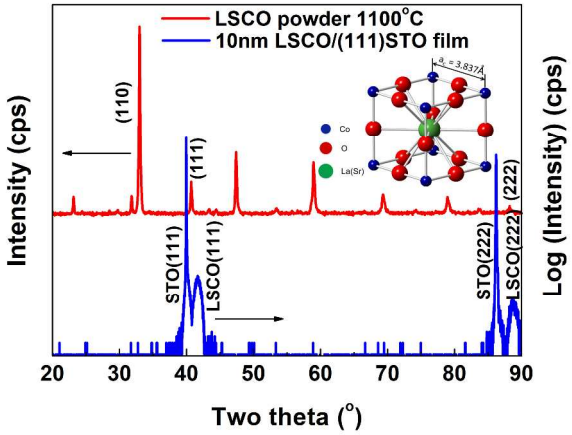

Figure 1. XRD pattern of as-synthesized $La_{0.5}Sr_{0.5}CoO_3$ powder (red line) and specular thin film XRD pattern from 10 nm LSCO thin film grown on STO (111) (blue line).

LSCO layers on STO (111). ICP-MS was used to check the composition of LSCO films and the ratio of La, Sr and Co is about 0.47:0.49:1, indicating a chemical formula of $La_{0.47}Sr_{0.49}CoO_{3-\delta}$ for the LSCO films. The specular XRD pattern from the 10-nm-thick LSCO film is demonstrated in **Figure 1** (lower line). The pattern shows diffraction lines of the (111) and (222) planes from both the LSCO film and STO (111) substrate, indicating that the LSCO film had a [111] out-of-plane crystal orientation. Comparison with the LSCO powder pattern (**Figure 1** upper line) shows a shift of the film peaks to larger 2θ angle, due to coherency strain caused by the negative lattice misfit (–1.7%) between LSCO and the substrate STO. The XRD in-plane scan and phi-scan at the LSCO $(1\bar{1}0)$ reflection are shown in **Figure 2**a-b. The in-plane scan reveals LSCO lattice planes normal to the thin film surface while phi-scan is an azimuthal scan at a fixed in-plane momentum transfer $Q_{//}$ corresponding to the $(1\bar{1}0)$ Bragg reflection of the LSCO film. Only $(1\bar{1}0)$ and $(2\bar{2}0)$ reflection peaks from both LSCO and STO appear and overlap. These results reveal that the LSCO film had a preferred $[1\bar{1}0]$ in-plane crystalline orientation with a sixfold symmetry indicated by the peak separation of 60^o, matching that of STO and demonstrating a "cube-on-cube" epitaxial relationship between LSCO and STO: LSCO {111} // STO {111}, $[1\bar{1}0]$ LSCO // $[1\bar{1}0]$ STO. A specular ω-rocking curve (RC) scan on peak LSCO (111) shown in **Figure 2**a inset reveals a full width at half maximum (FWHM) value of 0.07^o, which is close to values reported in literature for epitaxial LSCO thin films.[48] The specular ω-RC scan was conducted at a fixed specular momentum transfer $Q_{\perp}$ value corresponding to the (111) Bragg reflection of the LSCO film. These results reveal a strained and epitaxial LSCO film was synthesized with little defects and slight structural misorientations. Epitaxial LSCO thin films have been grown on various substrates using PLD; the present results are in good agreement with literature reports for LSCO on STO.[46,49] A low angle XRR profile of

the obtained LSCO film shown in **Figure 2**c reveals several interference fringes. The spectrum is plotted as a function of scattering vector $Q_z = 4\pi \sin\theta/\lambda$, where λ is the X-ray wavelength (1.5406 Å) and θ is the incident angle. The inset shows a fitting electron density profile of the LSCO film. The fit matches the data well for an LSCO film thickness of 98.3 Å, with interface and surface roughnesses of 5.1 Å and 6.2 Å, respectively. Surface morphology was examined by AFM with a 3D image and a line section profile (**Figure 2**d), indicating an LSCO surface RMS roughness of ≈ 7.0 Å, which is in the range desired to obtain high-quality XRR data.[50]

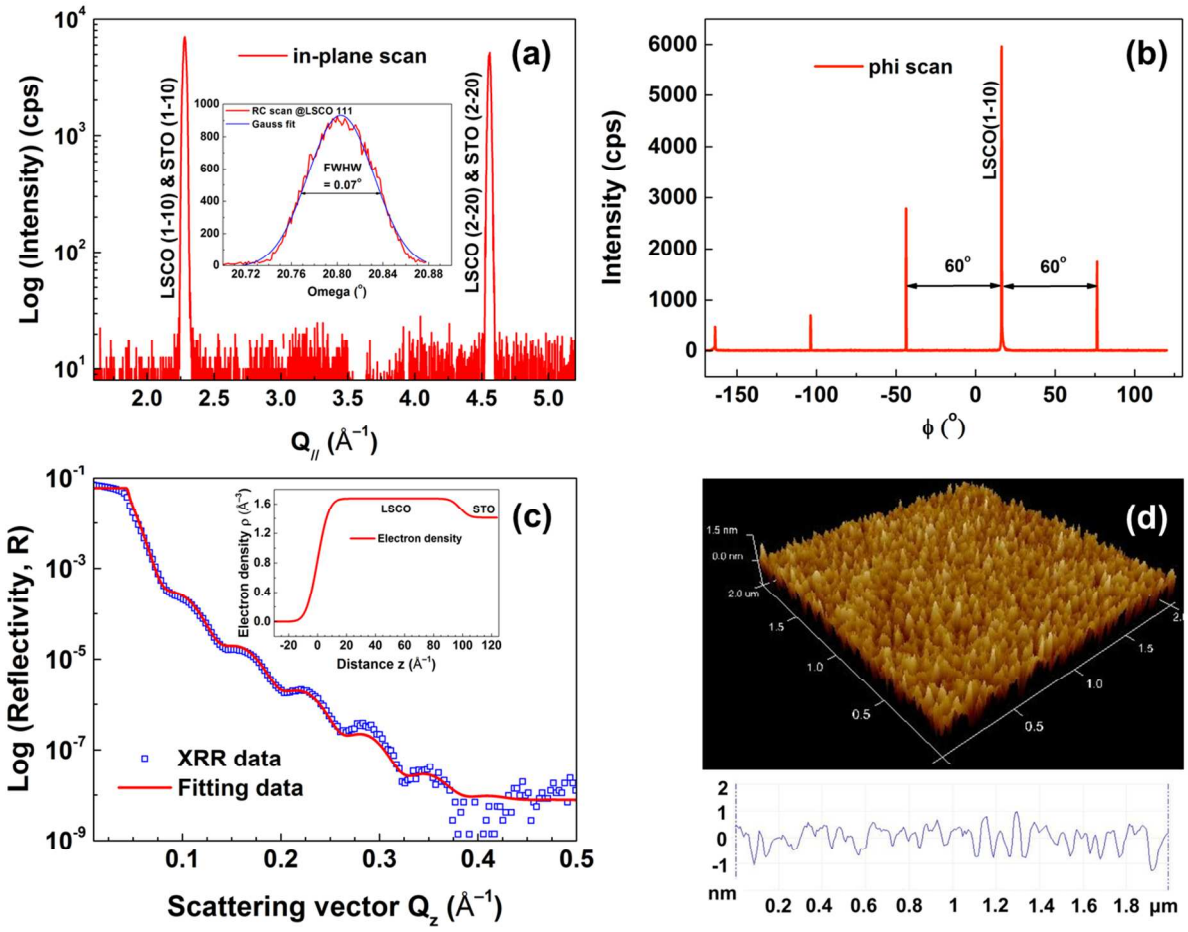

Figure 2. In-plane XRD (a) and phi-scan (b) patterns show the 10 nm LSCO/STO (111) thin film obtained in-plane epitaxy with $[1\bar{1}0]$ preferred orientation and a sixfold symmetry.

XRR spectrum with fitting curve and electron density profile (inset) for the LSCO film (c) and 3D AFM image with a line section profile (d) showing surface morphology of the LSCO film.

LMO on STO (111). LMO layers were grown on STO (111) by PLD to provide a comparison with LMO grown on LSCO-coated STO substrates. ICP-MS measurements show that the ratio of Li to Mn is about 0.68:2, indicating 32% Li was lost relative to the stoichiometric LMO target during the PLD process. Li loss is expected in LMO vapor deposition, especially given the present relatively large substrate-target separation (7.5 cm).[51] The loss of Li is not an issue for the use of these LMO films as a model system, because the Li content is still large enough to retain the correct spinel structure as indicated by the XRD and HRTEM results. In prior work on LMO thin films with similar low Li content, cyclic voltammograms showed the expected spinel Mn^{3+}/Mn^{4+} redox characteristics.[51] XRD patterns were obtained by thin-film X-ray diffraction (ATX-G, Rigaku). **Figures 3**a-b exhibit the specular, in-plane and phi-scan XRD patterns of a typical single layer LMO film with a thickness of around 27 nm. $Q_{\perp}$ and $Q_{//}$ in x-axis are specular and in-plane momentum transfers, respectively. The specular scan (red line in **Figure 3**a) shows 111, 222, 333, and 444 specular diffraction lines. The in-plane scan (blue line in **Figure 3**a) shows that the $[1\bar{1}0]$-type LMO reflections are aligned with the $[1\bar{1}0]$-type STO substrate reflections. A sixfold symmetry is indicated by the phi scan pattern at LMO $(4\bar{4}0)$ with an interval of 60^{o} shown in **Figure 3**b. A phi scan through the STO $(2\bar{2}0)$ reflections is also shown for comparison. These results clearly indicate that the LMO film was epitaxial on STO (111), with orientation relationship: LMO {111} // STO {111}, $[1\bar{1}0]$ LMO // $[1\bar{1}0]$ STO. The out-of-plane lattice constant of the LMO film determined from the (111)

reflection is 8.230 Å, indicating expansion was induced due to a positive lattice misfit (4.9% shown in **Table 2**) between LMO and STO. The low angle XRR data and fitting result shown in **Figure 3**c indicate that the interface and surface roughnesses are 2.6 Å and 11.7 Å, respectively. The AFM image and linear section profile (**Figure 3**d) indicate an RMS roughness of ≈ 12.0 Å.

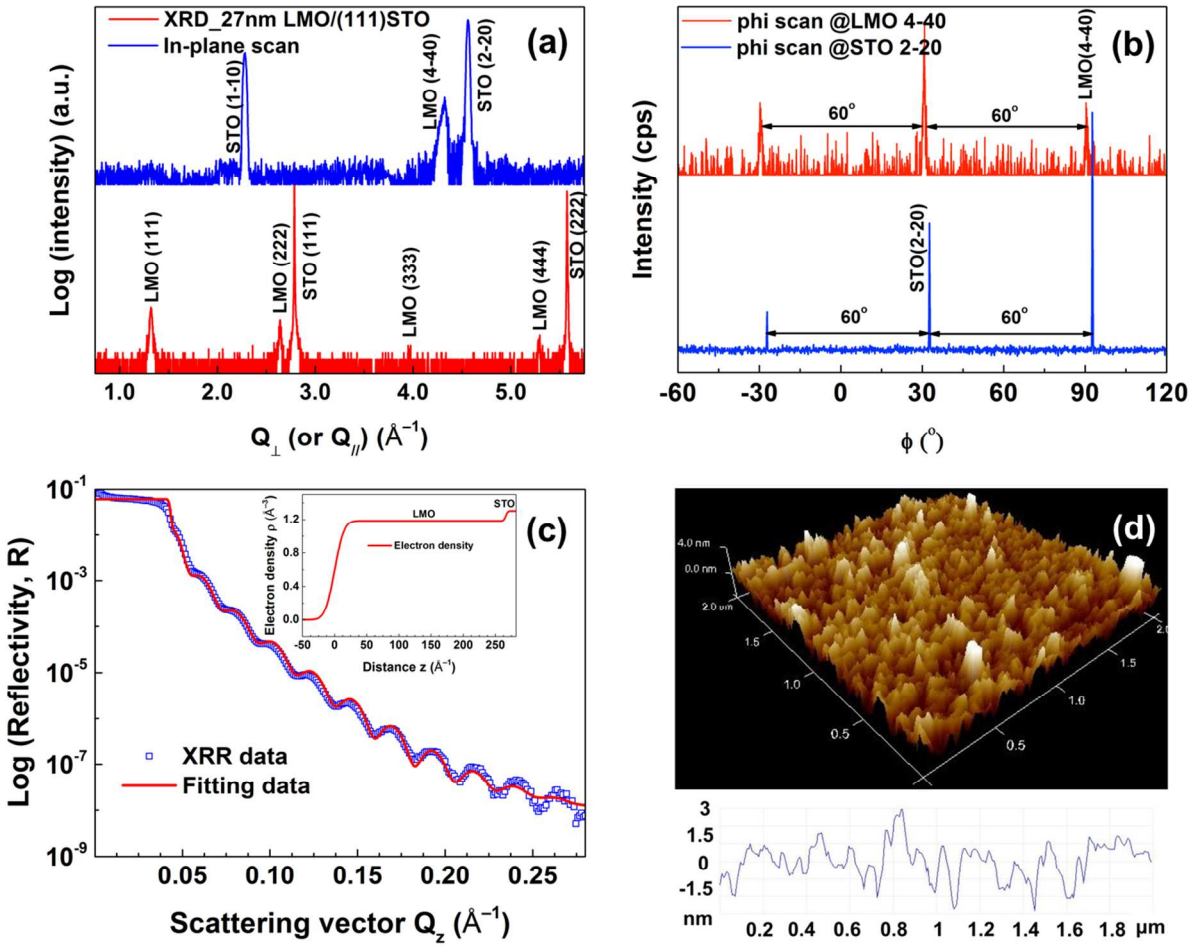

Figure 3. (a) Specular thin film XRD pattern (red line) from 27nm LMO thin film grown on STO (111) substrate. The pattern indicates [111] preferred specular orientation of the LMO film. In-plane XRD (blue line) shows that the LMO thin film exhibits in-plane epitaxy with $[1\bar{1}0]$ preferred orientation. (b) Phi scans of both LMO (red line) and STO (blue line) corresponding to the $(4\bar{4}0)$ and $(2\bar{2}0)$ reflections, respectively, indicate a sixfold symmetry

of the LMO film. (c) XRR spectrum with fitting curve and electron density profile (inset) for the LMO thin film, and 3D surface AFM image along with a line section profile (d) showing surface morphology of the LMO single layer film.

LMO/LSCO Bi-Layers on STO (111). Two different as-deposited LMO/LSCO bilayers were studied; the nominal LSCO thicknesses were 5 or 10 nm, while in both cases the nominal LMO thickness was 10 nm. According to the specular synchrotron XRD patterns in **Figure 4**a, both LMO and LSCO show (111) and (222) reflections, although the LSCO peaks are weaker and appear as a shoulder on the substrate peaks for the 5-nm-thick LSCO layer. This indicates [111] preferred specular orientation for both LMO and LSCO. In addition, the thin film XRD pattern of an in-plane scan is illustrated in **Figure 4**b, indicating a "cube-on-cube" epitaxial relationship was established: LMO {111} // LSCO {111} // STO {111}, $[1\bar{1}0]$ LMO // $[1\bar{1}0]$ LSCO // $[1\bar{1}0]$ STO, which is demonstrated by the inset in **Figure 4**a.

Bulk crystal structures and lattice constant values of LMO, LSCO and STO, along with XRD-measured lattice constant values and calculated lattice misfits for the 10 nm LMO/10 nm LSCO/STO bilayer are summarized in **Table 2**. The out-of-plane lattice constant of LMO, obtained from the (111) reflection in **Figure 4**a, is $a_{\perp}$ = 8.239 Å, which is larger than the bulk $Li_{0.68}Mn_2O_{4-\delta}$ lattice constant (~ 8.189 Å).[53] For LSCO, $a_{\perp}$ = 3.799 Å is obtained from the LSCO (111) reflection, which is, on the contrary, smaller than the bulk lattice constant (3.837 Å). **Figure 4**b shows the in-plane XRD scan, from which the in-plane lattice constants are acquired (shown in **Table 2**). The in-plane residual lattice misfits are then calculated to be 4.9% for LMO/LSCO and –0.1% for LSCO/STO. The extremely small LSCO/STO in-plane residual lattice misfit indicates that the LSCO was coherently strained

(expanded) to match the STO substrate lattice, whereas the out-of-plane lattice spacing contracted due to the Poisson effect. On the other hand, the LMO/STO lattice misfit is almost equal to the bulk lattice misfit, indicating that the LMO film was largely relaxed. This is consistent with the fact that the out-of-plane LMO lattice constant is only 0.6% larger than the bulk value.

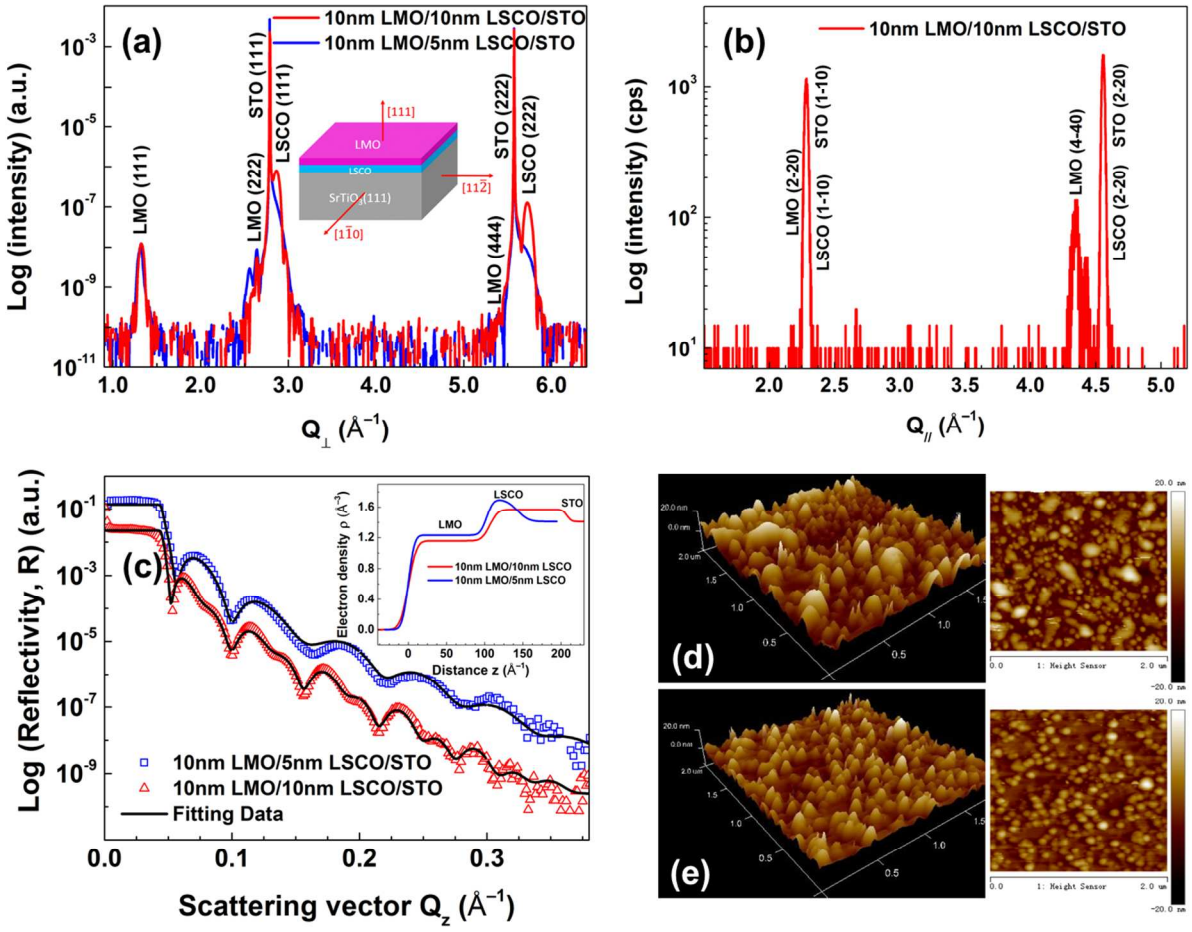

Figure 4. (a) Synchrotron XRD patterns from epitaxial LMO/LSCO bilayer thin films growing on STO (111). In-plane XRD (b) shows the LMO thin film obtained in-plane epitaxy with [1$\bar{1}$0] preferred orientation. (c) *Ex situ* XRR profiles for the hetero-epitaxial LMO/LSCO/STO (111) bilayer films. The fitting electron density profiles are shown in the inset. (d) and (e) Film morphology is exhibited by AFM images of the 10 nm LMO / 10 nm

LSCO bilayer and 10 nm LMO / 5 nm LSCO bilayer, respectively.

Table 2. Crystal structures, lattice constant values, and lattice misfits for $LiMn_2O_4$, $La_{0.5}Sr_{0.5}CoO_3$ and $SrTiO_3$ of bulk and thin film.

Target	Crystal structure	Bulk lattice constants (Å)	Specular lattice constants (Å)	In-plane lattice constants (Å)	Bulk lattice misfits	In-plane residual lattice misfits
LMO	$Fd\bar{3}m$	8.248[1]	8.239	8.184	LMO/STO 4.9%	LMO/STO 4.8%
LSCO	$Pm\bar{3}m$	3.837[2]	3.799	3.901	LMO/LSCO 6.7%	LMO/LSCO 4.9%
STO	$Pm\bar{3}m$	3.905	3.905	3.905	LSCO/STO –1.7%	LSCO/STO –0.1%

[1]Bulk lattice constant parameter for LMO with 0.68 Li is 8.189 Å, which is used for subsequent calculations.

[2]Pseudocubic lattice constant parameter for bulk LSCO.

XRR profiles from the as-grown bilayers, shown in **Figure 4c,** exhibit periodic broad Kiessig fringes. The XRR spectrum from 10 nm LMO / 10 nm LSCO bilayer shows a doubling of the periodicity as expected given the equal layer thicknesses, whereas the 10 nm LMO / 5 nm LSCO bilayer shows single asymmetric peaks. The XRR fittings also shown in **Figure 4**c indicate that the LMO surface roughness was < 1 nm for both bilayers. The fitting results also reveal that the thinner LSCO buffer layer results in a smaller LMO surface roughness. AFM images of the as-prepared bilayer surfaces are shown in **Figure 4**d and e, indicating the height and width of LMO surface undulations are smaller for the thinner LSCO buffer layer, in agreement with the XRR results. Moreover, the calculated electron density profiles (inset in **Figure 4**c) indicates thinner LSCO buffer layer (5 nm) can result in a denser LMO film with slightly higher electron density.

Cross-sectional TEM images of the 10 nm LMO / 10 nm LSCO bilayer are shown in **Figure 5**. A lower-magnification image (**Figure 5**a) illustrates that the LMO surface has periodic depressions. The inset is a higher-magnification view of one such depression in the LMO layer surface. A higher magnification view (**Figure 5**b) depicts the bi-layer hetero-structure where the interfaces are clearly visible; the LSCO layer had a reasonably uniform thickness resulting in a flat LSCO/LMO interface, unlike the rough LMO surface. **Figure 5**c is a high resolution TEM image taken along the $[1\bar{1}0]$ LMO // $[1\bar{1}0]$ LSCO // $[1\bar{1}0]$ STO direction where the continuity of the lattice fringes from STO (110), LSCO (110) and LMO (220) planes (marked in yellow lines) clearly illustrates the hetero-epitaxial bilayer structure. The d-spacings of the LMO (111) and LSCO (111) lattice planes are calculated from the reduced FFT diffraction patterns, also shown in **Figure 5**c. For the LMO layer, d_{111} = 4.8 Å, which is larger than the d-spacing value 4.728 Å for bulk $Li_{0.68}Mn_2O_{4-\delta}$. Similarly, d_{111} of LSCO is calculated to be around 2.2 Å, slightly smaller than the theoretical value, i.e. 2.215 Å. Those interplanar spacing differences reveal specular lattice expansion and contraction occurred in the LMO and LSCO layers, respectively. That is in accordance with the results of the XRD measurements in **Table 2** above. An enlarged HRTEM image (**Figure 5**d) depicts the LMO/LSCO hetero-interface with an overlaid diamond-shaped structure model indicating atom columns positions. The inset presents a computed projection of the Mn diamond configuration from ideal $LiMn_2O_4$ spinel structure, viewed along $[1\bar{1}0]$ orientation as the TEM images. The $[1\bar{1}0]$ cross-sectional projection is a special direction along which Li, Mn and O reside on completely separated atom columns from each other. This enables direct visualization of the hetero-interfaces through HRTEM imaging.[28,36] Moreover, the ratio of the shorter (m) and longer (n) diagonal lengths of the Mn diamond is a quick measurement of the structural distortion of LMO due to oxygen and lithium deficiencies at the hetero-

interface. The m/n ratio of LMO layer measured far beyond the LMO/LSCO interface shown in **Figure 5**d is around 0.71, which is close to the value for ideal cubic spinel LMO structure, i.e. 0.707.[28,37] However, the ratio at the LMO/LSCO interface is found to be ~0.74, which approximates that for tetragonal oxygen-deficient $Li_{1-x}Mn_2O_{4-\delta}$, i.e. 0.732 (the pseudo-cubic lattice parameters for tetragonal LMO are: a = b = 8.111 Å, c = 8.646 Å)[54]. It results in that the in-plane lattice misfit between LMO and LSCO at the interface is reduced to 4.0% from 6.7% (**Table 2**). The phase transformation from spinel cubic to tetragonal allowed layer-by-layer epitaxial LMO thin layer growth to be favored up to several monolayers above the LSCO surface by compensating for the lattice misfit strain. Far above the interface, the LMO crystal symmetry became spinel cubic, relaxed through misfit dislocations and 3D islands formation.

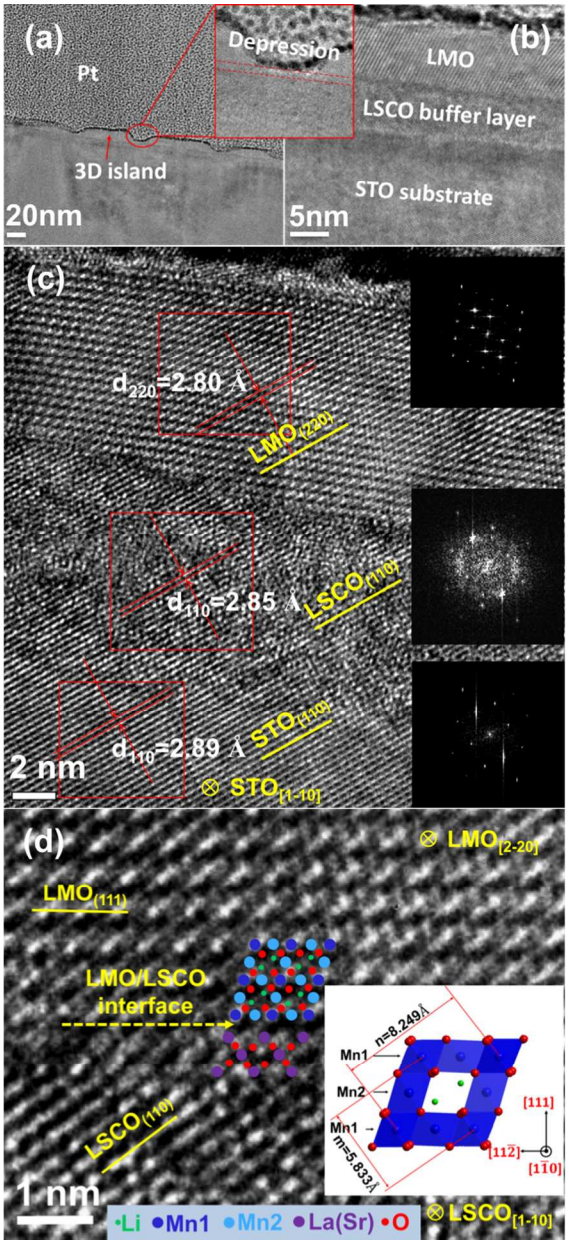

Figure 5. (a) and (b) TEM images showing hetero-structure of the 10 nm LMO / 10 nm LSCO / STO (111) bilayer film. 3D islands and depressions on LMO layer are illustrated in the enlarged inset. (c) Cross-sectional high resolution TEM image taken on the $(1\bar{1}0)$ plane along with reduced FFT diffraction patterns of LMO, LSCO and STO. (d) HRTEM image showing the LMO/LSCO hetero-interface. The overlaid diamond-shaped structure model indicates the atom columns positions. The inset is a projection of the diamond configuration

of ideal spinel LMO along [$1\bar{1}0$] direction, showing separate Li, O and Mn atom columns. Mn1 and Mn2 have different atom densities.

TEM-EDS elemental maps across the bilayer of the same TEM sample are shown in **Figure 6**a. Mn is detected only in LMO, whereas Co is present only in the LSCO layer. Sr distributes across both LSCO and STO substrate. La is mostly present in the LSCO layer; the La signal in the STO layer is an artifact due to peak overlap with Ti. The TEM results for LSCO grown on STO indicate that the layer remained coherently strained with a sub-nano flat surface. This suggests a layer-by-layer Frank–van der Merwe (FM) growth mode due to the relatively small LSCO/STO lattice misfit, i.e. –1.7%. The lack of strain relaxation is reasonably consistent with Matthews-Blakeslee theory for relaxation due to misfit dislocations, applied to oxide materials at these thickness and mismatch values.[55,56] With rational and ideal assumptions (pure edge dislocations, Poisson ratio of LSCO ~ 0.3, burger's vector equals in-plane d-spacing), the critical thickness of strained LSCO film is about 2 nm according to Matthews-Blakeslee optimal relaxation theory.[17] The 10 nm LSCO film here continued to maintain epitaxy by forming misfit dislocations beyond the calculated critical thickness. On the other hand, for LMO grown on LSCO-coated STO, the layers were mostly relaxed and showed periodic depressions or undulations; such roughening is commonly observed due to the large mismatch between LMO and these substrates or the underlying layer,[23,24] suggesting Stranski-Krastanov (SK) mode growth.[57] In this mode, a thin flat film forms initially, followed by an instability in the growth front that leads to large surface roughness; the enlarged inset in **Figure 5**a appears to show that a thin initial layer of LMO (~2nm) is present on the LSCO layer beneath the depression. In this region, relaxation of the coherency strain probably occurs by a combination of misfit dislocations and depressions on the rough film surface.[57,58] To further verify the different thin film

growth mechanisms, **Figure 6**b shows an enlarged HRTEM image from **Figure 5**c, revealing a dislocation, labeled "T", at the LMO/LSCO (111) interface with the Burger's vector perpendicular to the LMO (220) planes. The dislocation is more visible in the inverse FFT-filtered image shown in **Figure 6**c. In contrast, no dislocations are discerned at the LSCO/STO (111) interface (**Figure 6**d), indicating a coherently-strained LSCO layer as expected due to the small lattice misfit.

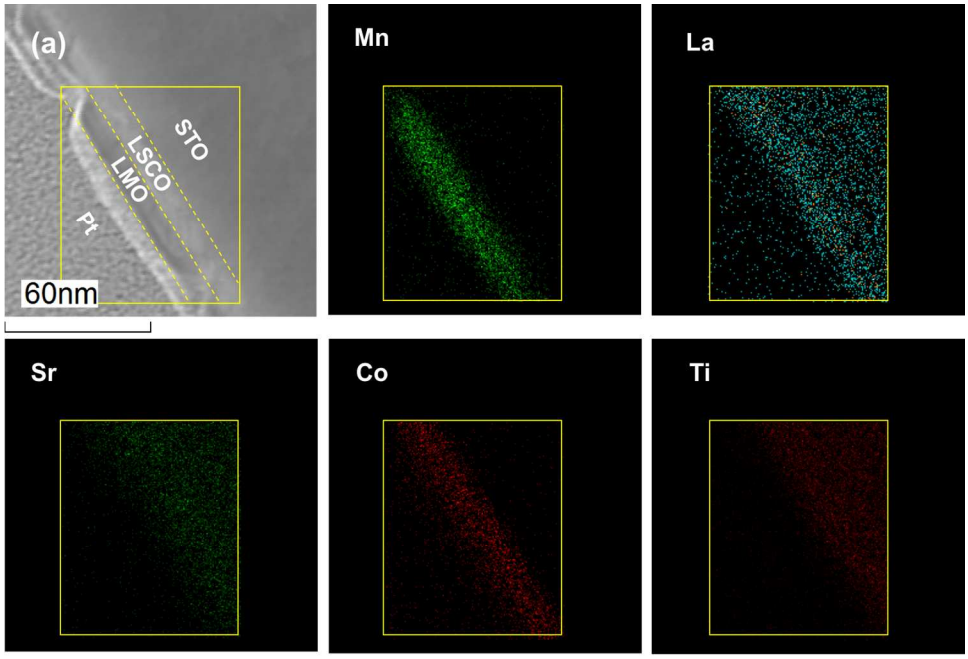

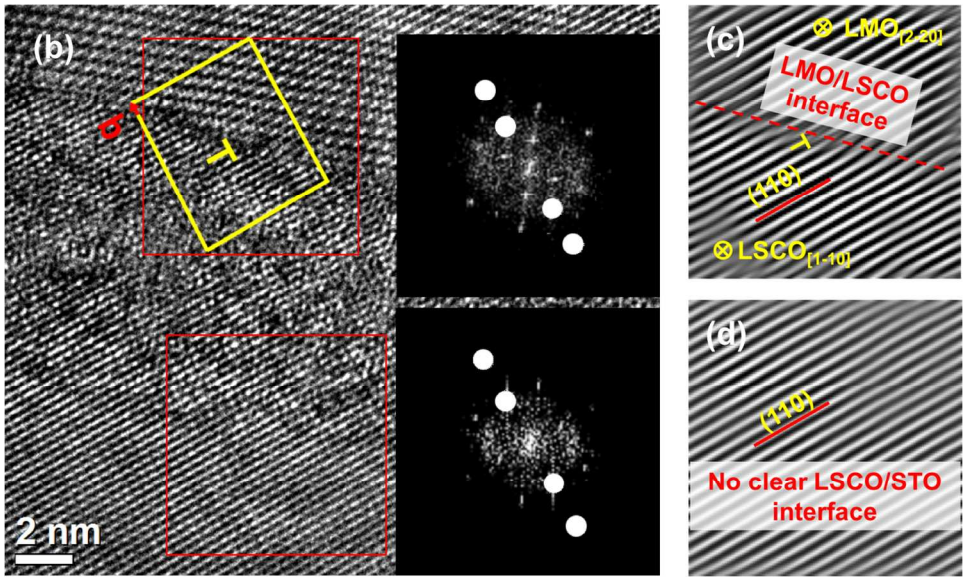

Figure 6. (a) Cross-sectional EDS elemental mapping on the TEM sample of LMO/LSCO/STO (111) bilayer thin film. (b) Cross-sectional HRTEM images taken along the $[1\bar{1}0]$ LMO // $[1\bar{1}0]$ LSCO // $[1\bar{1}0]$ STO direction showing hetero-interfaces of the 10 nm LMO / 10 nm LSCO/STO (111) bilayer. A dislocation labeled "T" was formed at the LMO/LSCO interface. Insets are reduced FFT diffraction patterns of the LMO/LSCO and LSCO/STO interfaces, respectively. (c) and (d) exhibit inverse reduced FFT images of the LMO (220) (440), LSCO and STO (110) (220) planes circled in the insets in (b), clearly showing a dislocation at the LMO/LSCO interface.

Synchrotron low angle XRR profiles for the 10 nm LMO / 10 nm LSCO bilayer before, during and after cycling are shown in **Figure 7**a. The dramatically different XRR curves after both the thin film was soaked in electrolyte and 1st cycle indicate notable interface structure and/or morphology changes between LMO and the liquid electrolyte. The similar XRR profiles after 1st and 3rd cycles indicate that the surface morphology of LMO did not evolve significantly beyond the first cycle. A four-layer model including STO, LSCO, LMO, and SEI (inset in **Figure 7**a) was applied to fit the XRR spectra using Motofit package in

Igor Pro software. Part of the fitting results are shown in **Table 3**. Significant shape changes of the XRR spectra resulted from thickness and surface morphology changes of the SEI layer between the LMO surface and the liquid electrolyte. An ~ 3.3 nm SEI layer, assumed to consist of low density lithium salts and various organic compounds, was formed after LMO contacted with the electrolyte solution, in agreement with prior reports for epitaxial LMO thin films.[7,8,13] The refined electron density of this SEI layer is 0.0413 $Å^{-3}$, similar to previously reported values.[8,24] In addition, the fitting results indicate that the SEI layer became thicker and rougher after 3 cycles, while the LMO (111) surface morphology stayed relatively stable. The 2D intensity spectra from *in situ* Synchrotron XRD during the first 3 cycles is shown in **Figure 7**b for the LMO (111) Bragg peak. The LMO (111) peak position irreversibly shifts to lower Q value after the first cycle and then stays nearly constant, indicating that the LMO redox reaction almost stopped after the first cycle.

Table 3. Parameters obtained by fitting the *in situ* XRR data from the 10nm LMO/10nm LSCO/STO bilayer. (unit: Å)

Conditions	SEI layer		LMO		LSCO		STO	
	thickness	roughness	thickness	roughness	thickness	roughness	thickness	roughness
As-deposited	-	-	108.6	8.1	99.7	8.3	-	7.9
As-assembled	32.9	11.5	105.2	6.8	95.2	7.9	-	9.3
After 1st cycle	43	15.9	100.4	6	98.4	25.2	-	6.1
After 3rd cycle	50.9	20.3	91.1	6.5	93.4	27.9	-	6.2

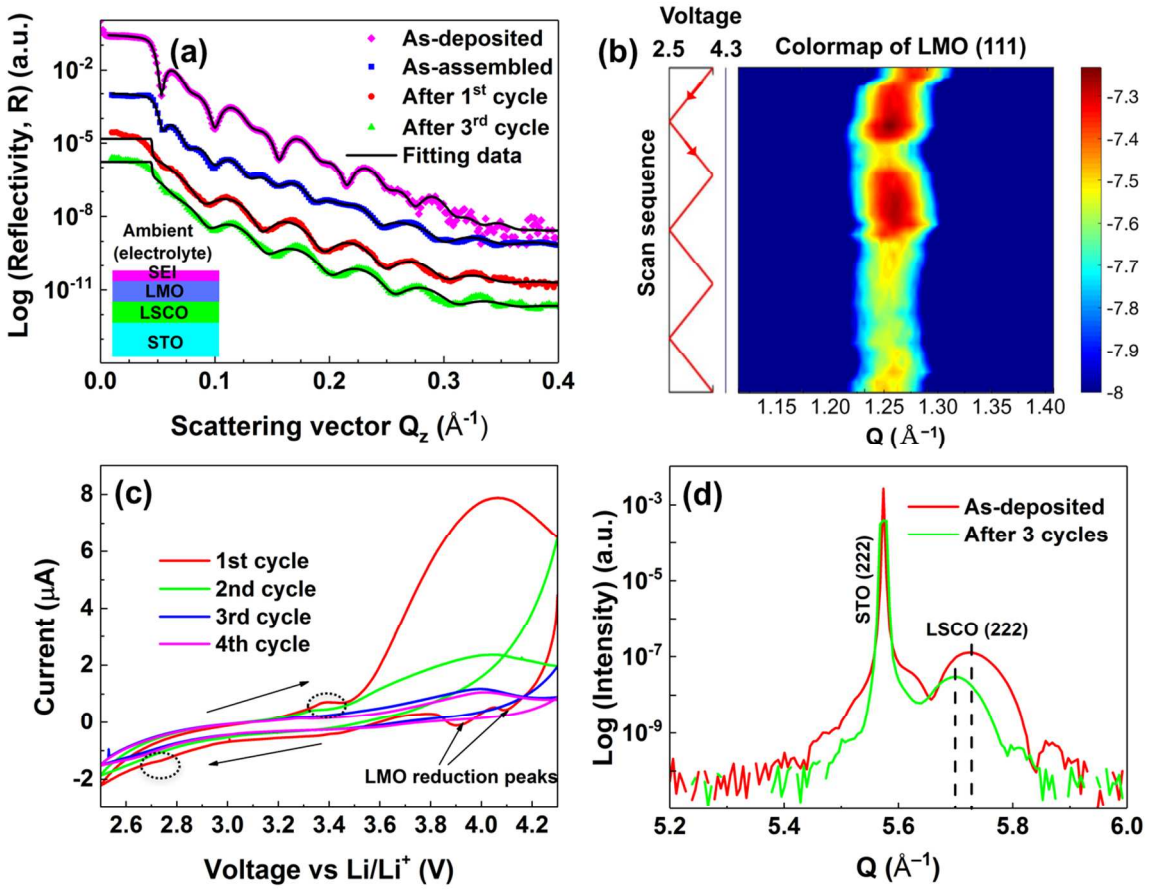

Figure 7. (a) XRR profiles by synchrotron X-ray scattering for the 10 nm LMO / 10 nm LSCO bilayer films of as-deposited, as-assembled, after 1st and 3rd cycles. The profiles are vertically offset in order to make clear comparison. The inset shows a four-layer model used to fit the XRR spectra. (b) 2D intensity spectra from *in situ* synchrotron XRD of LMO (111) peak during 3 voltammetric cycles between 2.5V to 4.3V at potential intervals of 0.5 mV/s. (c) Cyclic voltammetry of a 10 nm LMO / 10 nm LSCO/STO (111) bilayer thin film between 2.5V to 4.3V at potential intervals of 0.5 mV/s. The Mn^{3+}/Mn^{2+} redox peaks around the 3.0 V plateau are circled by two black dashed circles. (d) Synchrotron XRD of LSCO peak (222) from the 10 nm LMO/10 nm LSCO/STO (111) bilayer. The peak slightly shifted to lower Q after 3 voltammetry cycles.

Cyclic voltammetry profiles over the first four cycles of the 10nm LMO / 10nm LSCO bilayer are shown in **Figure 7**c where redox peaks are present for the first cycle. Data began to be obtained after charging the cell to 4.3V. The 0.5 mV/s potential sweep rate was slow enough to get good cyclic voltammetry resolution for very thin (10 nm) LMO layers, as indicated by the LMO reduction peaks observed in the first cycle.[51] Two reduction peaks coming from LMO are clearly identified during the first discharge reaction at Mn^{3+}/Mn^{4+} cathodic plateaus. During the following charge process, a very broad redox peak resides at a voltage of around 4.1V, which is not typical for LMO and obscures the LMO Mn^{3+}/Mn^{4+} anodic peaks. The net charge obtained by integrating over this peak is much larger than the charge from complete delithiation of the LMO layer. The additional charge associated with this peak may originate from a change in oxygen content of the LSCO layer. Indeed, the observed excess charge can be explained by an ~ 50% change in the lattice oxygen content in the LSCO buffer layer. After the first cycle, little if any redox reactions are detected from either LMO or LSCO. This is in apparent agreement with the result in **Figure 7**b, where LMO X-ray peak shifts only in the first cycle. Subsequent electrical sheet resistance measurements show a significant decrease in LSCO electrical conductivity by around 10 times. These results suggest that the initial charging process caused irreversible changes in the LSCO, resulting in the decreased conductivity, which prevented further LMO redox reactions. In addition, the LMO Mn^{2+}/Mn^{3+} redox peaks can be identified around the 3.0 V plateau during the first cycle, marked by two black dashed circles. The redox peak positions are similar to those reported for LMO thin films in the literature,[51] but the peaks are weak and poorly resolved. The broad weak peak shape was probably caused by structural defects, similar to prior results for $LiNiVO_4$ thin films.[60]

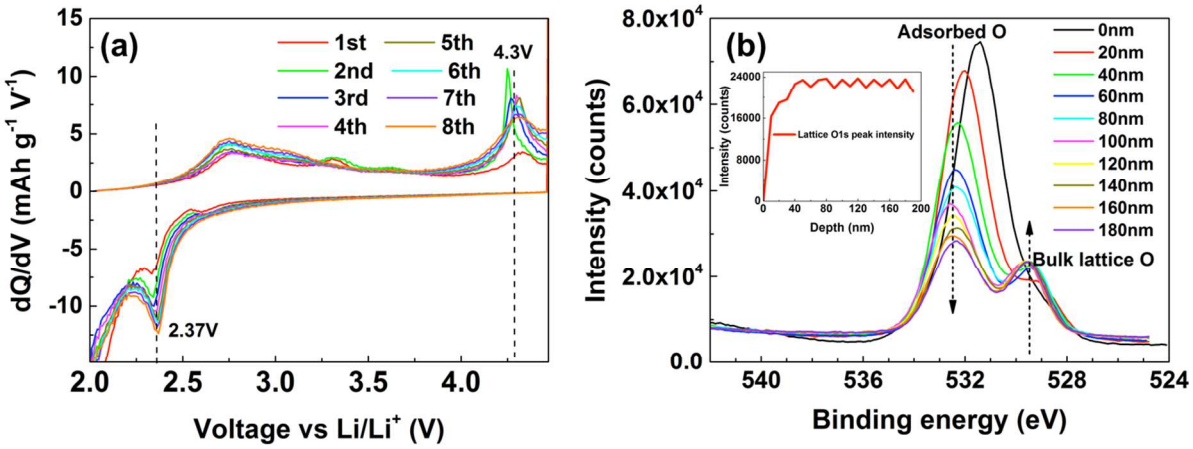

Figure 8. (a) Galvanostatic cycling test on LSCO powder as active cathode materials between 2.0V to 4.5V using a current density of 10 μA/g. (b) XPS depth profile of doublet O1s peak from LSCO powder after 100 galvanostatic cycles. The inset shows a depth profile of the bulk lattice O1s peak intensity.

To further examine the electrochemical characteristics of LSCO, synthesized LSCO powder was used as the active cathode material in a half-cell, and galvanostatically cycled between 2.0V to 4.5V at a current density of 10 μA/g; the results are shown in **Figure 8**a. One oxidation peak at 4.3V is found, which is similar to the anodic peak around 4.1V of the LSCO/LMO bilayer at the first charge process (**Figure 7**c). One reduction peak at 2.37V is also identified. It is inferred that those two redox peaks are in coincidence with oxygen reduction and evolution reactions in a lithium-air battery cathode with LSCO as catalysts (ORR: $O_2 + Li^+ + e^- = LiO_2$, $LiO_2 + Li^+ + e^- = Li_2O_2$).[61] Therefore, the oxygen evolution reaction during the first charge process of the LSCO/LMO bilayers resulted in LSCO lattice oxygen loss which cannot be restored due to low oxygen content in the glovebox (<1 ppm). In consequence, electrical conductivity of LSCO is dramatically reduced ascribed to increased oxygen vacancy concentration.[41] **Figure 7**d shows the LSCO 222 peak from the

10 nm LMO / 10 nm LSCO/STO bilayer irreversibly shifted to lower Q value after 3 cycles, also indicating oxygen loss in LSCO along with a lattice spacing increase. To further verify the aforementioned LSCO lattice oxygen loss interpretation, XPS depth profiling was done on cycled LSCO powder. The evolution of the doublet O1s peak along a depth range of 190 nm is exhibited in **Figure 8**b. Two O1s peak positions with binding energy (BE) values of around 529.5 eV and 532.5 eV were identified. The peak with higher BE value is generally accepted as adsorbed oxygen while the peak with lower BE value is attributed to be the weak metal-oxygen bond (bulk lattice oxygen).[62,63] The inset shows the peak intensity of the bulk lattice O1s as a function of sputtering depth. It can be seen that the peak intensity keeps almost constant after a rapid increase over the first 40 nm of depth, indicating significant lattice oxygen loss at the outermost surface of the electrochemically cycled LSCO powder. These results, taken together, strongly suggest that oxygen loss during cycling led to a dramatic electrical conductivity loss of the LSCO powder, which is not desired for a conductive buffer layer material.

4. CONCLUSIONS

In summary, hetero-epitaxial LMO/LSCO bilayer thin films have been grown on STO (111) substrates using PLD. *Ex situ* XRD and XRR measurements verified successful synthesis of 10 nm epitaxial LMO thin films. LMO/LSCO bilayers had a "cube-on-cube" epitaxial relationship with the STO substrates. It was demonstrated that a thinner LSCO buffer layer favored lower LMO surface roughness. Cross-sectional high resolution TEM imaging of the bilayer thin films indicated a Stranski-Krastanov (SK) growth mode of LMO layers on which 3D islands and depressions were formed due to the large lattice mismatch between LMO and the underlying LSCO/STO. Misfit dislocations at the LMO/LSCO hetero-interface were discerned through HRTEM. A phase transformation from cubic spinel LMO

to tetragonal oxygen-deficient LMO was observed at the LMO/LSCO interface, suggesting epitaxial LMO growth was facilitated by an interface structural distortion to reduce lattice misfit strain. The overall crystal quality and surface flatness of the hetero-epitaxial LMO/LSCO bilayer thin films was generally comparable or better than observed for other back-contact materials. Significant changes of the bilayer XRR profiles after battery assembly indicates formation of a SEI layer (~3.3 nm by XRR refinement) which got thicker and rougher after cycling while the LMO (111) surface morphology stayed relatively stable.

In situ synchrotron XRD measurements showed clear characteristics of LMO redox reactions which, however, stopped after the first cycle, consistent with the cyclic voltammetry results showing no apparent redox peaks after first discharge step. A probable explanation is that the buffer layer LSCO lost electrical conductivity due to lattice oxygen loss during the first charge process, which is further verified by a severely reduced intensity of the bulk lattice XPS O1s peak at the outermost layer (40nm) of electrochemically cycled LSCO powder. Despite this issue, further studies of LSCO may still be warranted because of the general difficulty of finding a good epitaxial conducting back-contact layer. As discussed in the Introduction, various approaches have been reported including Nb:$SrTiO_3$ substrates and various conducting-layer / substrate systems. All of these, with the possible exception of $SrRuO_3$, have shown problems with conductivity loss or poor LMO epitaxy due to three-dimensional island formation or poor crystal quality. A possible avenue for future work can be seen by noting that LSCO layer retain ~ 10% of their original conductivity after electrochemical cycling. Thus, increasing the LSCO layer thickness may provide sufficient electrical connection to allow good cycling characteristics.

AUTHOR INFORMATION

Corresponding Author

*E-mail: s-barnett@northwestern.edu (S.A.B.). Phone: (847) 491-2447.

Notes

The authors declare no competing financial interest.

ACKNOWLEDGMENTS

This work was supported as part of the Center for Electrochemical Energy Science, an Energy Frontier Research Center funded by the U.S. Department of Energy, Office of Science, Basic Energy Sciences (DE- AC02-06CH11357). Research at the Advanced Photon was supported by DOE, Office of Science, BES. This work made use of the EPIC, Keck-II, and/or SPID facility(ies) of Northwestern University's NUANCE Center, which has received support from the Soft and Hybrid Nanotechnology Experimental (SHyNE) Resource (NSF ECCS-1542205); the MRSEC program (NSF DMR-1121262) at the Materials Research Center; the International Institute for Nanotechnology (IIN); the Keck Foundation; and the State of Illinois, through the IIN. This work also made use of Pulsed Laser Deposition Shared Facility at the Materials Research Center at Northwestern University supported by the National Science Foundation's MRSEC program (DMR-1121262).

REFERENCES

(1) Scrosati, B.; Garche, J. Lithium Batteries: Status, Prospects and Future. *J. Power Sources* **2010**, *195*, 2419−2430.

(2) Goodenough, J. B.; Park, K. S. The Li-Ion Rechargeable Battery: a Perspective. *J. Am. Chem. Soc.* **2013**, *135*, 1167−1176.

(3) Manthiram, A. Materials Challenges and Opportunities of Lithium Ion Batteries. *J. Phys. Chem. Lett.* **2011**, *2*, 176−184.

(4) Fergus, J. W. Recent Developments in Cathode Materials for Lithium Ion Batteries. *J. Power Sources* **2010**, *195*, 939−954.

(5) Tarascon, J. M.; Armand, M. Issues and Challenges Facing Rechargeable Lithium Batteries. *Nature* **2001**, *414*, 359−367.

(6) Gummow, R. J.; De Kock, A.; Thackeray, M. M. Improved Capacity Retention in Rechargeable 4V Lithium/Lithium-Manganese Oxide (spinel) Cells. *Solid State Ionics*, **1994**, *69*, 59−67.

(7) Lu, J.; Zhan, C.; Wu, T.; Wen, J.; Lei, Y.; Kropf, A. J.; Wu, H.; Miller, D.J.; Elam, J.W.; Sun, Y.K; Qiu, X. Effectively Suppressing Dissolution of Manganese from Spinel Lithium Manganate via a Nanoscale Surface-Doping Approach. *Nat. Commun.* **2014**, *5*.

(8) Hirayama, M.; Sonoyama, N.; Ito, M.; Minoura, M.; Mori, D.; Yamada, A.; Tamura, K.; Mizuki, J.I.; Kanno, R. Characterization of Electrode/Electrolyte Interface with X-ray Reflectometry and Epitaxial-Film $LiMn_2O_4$ Electrode. *J. Electrochem. Soc.* **2007**, *154*, A1065−A1072.

(9) Yi, X.; Wang, X.; Ju, B.; Shu, H.; Wen, W.; Yu, R.; Wang, D.; Yang, X. Effective Enhancement of Electrochemical Performance for Spherical Spinel $LiMn_2O_4$ via Li Ion Conductive Li_2ZrO_3 Coating. *Electrochim. Acta* **2014**, *134*, 143−149.

(10) Gauthier, M.; Carney, T.J.; Grimaud, A.; Giordano, L.; Pour, N.; Chang, H.H.; Fenning, D.P.; Lux, S.F.; Paschos, O.; Bauer, C.; Maglia, F. Electrode–Electrolyte Interface in Li-Ion Batteries: Current Understanding and New Insights. *J. Phys. Chem. Lett*. **2015**, *6,* 4653−4672.

(11) Abe, T.; Fukuda, H.; Iriyama, Y.; Ogumi, Z. Solvated Li-ion Transfer at Interface between Graphite and Electrolyte. *J. Electrochem Soc*. **2004**, *151,* A1120–A1123.

(12) Haruta, M.; Shiraki, S.; Ohsawa, T.; Suzuki, T.; Kumatani, A.; Takagi, Y.; Shimizu, R.; Hitosugi, T. Preparation and in-situ Characterization of Well-defined Solid Electrolyte/Electrode Interfaces in Thin-Film Lithium Batteries. *Solid State Ionics*, **2016**, *285*, 118−121.

(13) Takada, K. Progress and Prospective of Solid-State Lithium Batteries. *Acta Mater.* **2013**, *61*, 759−770.

(14) Put, B.; Vereecken, P.M.; Labyedh, N.; Sepulveda, A.; Huyghebaert, C.; Radu, I.P.; Stesmans, A. High Cycling Stability and Extreme Rate Performance in Nanoscaled $LiMn_2O_4$ Thin Films. *ACS Appl. Mater. Interfaces* **2015**, *7*, 22413−22420.

(15) Miikkulainen, V.; Ruud, A.; Østreng, E.; Nilsen, O.; Laitinen, M.; Sajavaara, T.; Fjellvåg, H. Atomic Layer Deposition of Spinel Lithium Manganese Oxide by Film-Body-Controlled Lithium Incorporation for Thin-Film Lithium-Ion Batteries. *J. Phys. Chem. C* **2013**, *118*, 1258−1268.

(16) Liu, J.; Sun, X. Elegant Design of Electrode and Electrode/Electrolyte Interface in Lithium-Ion Batteries by Atomic Layer Deposition. *Nanotechnology* **2014**, *26*, 024001.

(17) Ohring, M. *Materials Science of Thin Films: Deposition and Structure,* 2nd ed; Academic press: San Diego, CA, **2001**.

(18) Sonoyama, N.; Iwase, K.; Takatsuka, H.; Matsumura, T.; Imanishi, N.; Takeda, Y.; Kanno, R. Electrochemistry of $LiMn_2O_4$ Epitaxial Films Deposited on Various Single Crystal Substrates. *J. Power Sources* **2009**, *189*, 561−565.

(19) Kim, S.; Hirayama, M.; Suzuki, K.; Kanno, R. Hetero-Epitaxial Growth of $Li_{0.17}La_{0.61}TiO_3$ Solid Electrolyte on $LiMn_2O_4$ Electrode for All Solid-State Batteries. *Solid State Ionics* **2014**, *262*, 578−581.

(20) Zeng, Z.; Liang, W.I.; Liao, H.G.; Xin, H.L.; Chu, Y.H.; Zheng, H. Visualization of Electrode–Electrolyte Interfaces in $LiPF_6$/EC/DEC Electrolyte for Lithium Ion Batteries via in situ TEM. *Nano Lett.* **2014**, *14*, 1745−1750.

(21) Lee, S.; Oshima, Y.; Hosono, E.; Zhou, H.; Kim, K.; Chang, H.M.; Kanno, R.; Takayanagi, K. In situ TEM Observation of Local Phase Transformation in a Rechargeable $LiMn_2O_4$ Nanowire Battery. *J. Phys. Chem. C* **2013**, *117*, 24236−24241.

(22) Harks, P.P.R.M.L.; Mulder, F.M.; Notten, P.H.L. In situ Methods for Li-Ion Battery Research: A Review of Recent Developments. *J. Power Sources* **2015**, *288*, 92−105.

(23) Suzuki, K.; Kim, K.; Taminato, S.; Hirayama, M.; Kanno, R. Fabrication and Electrochemical Properties of $LiMn_2O_4/SrRuO_3$ Multi-Layer Epitaxial Thin Film Electrodes. *J. Power Sources* **2013**, *226*, 340−345.

(24) Hirayama, M.; Ido, H.; Kim, K.; Cho, W.; Tamura, K.; Mizuki, J.I.; Kanno, R. Dynamic Structural Changes at $LiMn_2O_4$/Electrolyte Interface during Lithium Battery Reaction. *J. Am. Chem. Soc.* **2010**, *132*, 15268−15276.

(25) Kim, J.S.; Kim, K.; Cho, W.; Shin, W.H.; Kanno, R.; Choi, J.W. A Truncated Manganese Spinel Cathode for Excellent Power and Lifetime in Lithium-Ion Batteries. *Nano Lett.* **2012**, *12*, 6358−6365.

(26) Kim, S.; Aykol, M.; Wolverton, C. Surface Phase Diagram and Stability of (001) and (111) $LiMn_2O_4$ Spinel Oxides. *Phys. Rev. B* **2015**, *92*, 115411.

(27) Wei, J.; Ogawa, D.; Fukumura, T.; Hirose, Y.; Hasegawa, T. Epitaxial Strain-Controlled Ionic Conductivity in Li-Ion Solid Electrolyte $Li_{0.33}La_{0.56}TiO_3$ Thin Films. *Cryst. Growth Des.* **2015**, *15*, 2187−2191.

(28) Ikuhara, Y.H.; Gao, X.; Huang, R.; Fisher, C.A.; Kuwabara, A.; Moriwake, H.; Kohama, K. Epitaxial Growth of $LiMn_2O_4$ Thin Films by Chemical Solution Deposition for Multilayer Lithium-Ion Batteries. *J. Phys. Chem. C* **2014**, *118*, 19540−19547.

(29) Shiraki, S.; Takagi, Y.; Shimizu, R.; Suzuki, T.; Haruta, M.; Sato, Y.; Ikuhara, Y.; Hitosugi, T. Orientation Control of $LiCoO_2$ Epitaxial Thin Films on Metal Substrates. *Thin Solid Films* **2016**, *600*, 175−178.

(30) Kumatani, A.; Shiraki, S.; Takagi, Y.; Suzuki, T.; Ohsawa, T.; Gao, X.; Ikuhara, Y.; Hitosugi, T. Epitaxial Growth of $Li_4Ti_5O_{12}$ Thin Films Using RF Magnetron Sputtering. *Jpn. J. Appl. Phys.* **2014**, *53*, 058001.

(31) Kim, S.; Hirayama, M.; Taminato, S.; Kanno, R. Epitaxial Growth and Lithium Ion Conductivity of Lithium-Oxide Garnet for an All Solid-State Battery Electrolyte. *Dalton Trans.* **2013**, *42*, 13112−13117.

(32) Shiraki, S.; Takagi, Y.; Shimizu, R.; Suzuki, T.; Haruta, M.; Sato, Y.; Ikuhara, Y.; Hitosugi, T. Orientation Control of $LiCoO_2$ Epitaxial Thin Films on Metal Substrates. *Thin Solid Films*, **2016**, *600*, 175−178.

(33) Shiraki, S.; Oki, H.; Takagi, Y.; Suzuki, T.; Kumatani, A.; Shimizu, R.; Haruta, M.; Ohsawa, T.; Sato, Y.; Ikuhara, Y.; Hitosugi, T. Fabrication of All-Solid-State Battery Using Epitaxial $LiCoO_2$ Thin Films. *J. Power Sources* **2014**, *267*, 881−887.

(34) Halley, D.; Rossel, C.; Widmer, D.; Wolf, H.; Gariglio, S. Thermal Stability of $SrRuO_3$ Epitaxial Layers under Forming-Gas Anneal. *Mater. Sci. Eng., B* **2004**, *109*, 113−116.

(35) Bouchard, R.J.; Gillson, J.L. Electrical Properties of $CaRuO_3$ and $SrRuO_3$ Single Crystals. *Mater. Res. Bull.* **1972**, *7*, 873−878.

(36) Gao, X.; Ikuhara, Y. H.; Fisher, C. A.; Moriwake, H.; Kuwabara, A.; Oki, H.; Kohama, K.; Yoshida, R.; Huang, R.; Ikuhara, Y. Structural Distortion and Compositional Gradients Adjacent to Epitaxial $LiMn_2O_4$ Thin Film Interfaces. *Adv. Mater. Interface* **2014**, *1,* 1400143.

(37) Huang, R.; Ikuhara, Y.H.; Mizoguchi, T.; Findlay, S.D.; Kuwabara, A.; Fisher, C.A.; Moriwake, H.; Oki, H.; Hirayama, T.; Ikuhara, Y. Oxygen-Vacancy Ordering at Surfaces of Lithium Manganese (III, IV) Oxide Spinel Nanoparticles. *Angew. Chem. Int. Ed.* **2011**, *50*, 3053−3057.

(38) Reddy, M.V.; Sakunthala, A.; SelvashekaraPandian, S.; Chowdari, B.V.R. Preparation, Comparative Energy Storage Properties, and Impedance Spectroscopy Studies of Environmentally Friendly Cathode, $Li(MMn_{11/6})O_4$ (M= $Mn_{1/6}$, $Co_{1/6}$,($Co_{1/12}Cr_{1/12}$)). *J. Phys. Chem. C* **2013**, *117*, 9056−9064.

(39) Reddy, M.V.; Raju, M.S.; Sharma, N.; Quan, P.Y.; Nowshad, S.H.; Emmanuel, H.C.; Peterson, V.K.; Chowdari, B.V.R. Preparation of $Li_{1.03}Mn_{1.97}O_4$ and $Li_{1.06}Mn_{1.94}O_4$ by the Polymer Precursor Method and X-ray, Neutron Diffraction and Electrochemical Studies. *J. Electrochem. Soc.* **2011**, *158*, A1231−A1236.

(40) Reddy, M.V.; Manoharan, S.S.; John, J.; Singh, B.; Rao, G.S.; Chowdari, B.V.R. Synthesis, Characterization, and Electrochemical Cycling Behavior of the Ru-Doped Spinel, $Li[Mn_{2-x}Ru_x]O_4$ (x= 0, 0.1, and 0.25). *J. Electrochem. Soc.* **2009**, *156*, A652−A660.

(41) Mitberg, E.B.; Patrakeev, M.V.; Leonidov, I.A.; Kozhevnikov, V.L; Poeppelmeier, K.R. High-Temperature Electrical Conductivity and Thermopower in Nonstoichiometric $La_{1-x}Sr_xCoO_{3-\delta}$ (x= 0.6). *Solid State Ionics* **2000**, *130*, 325−330.

(42) Xie, Q.Y.; Wu, Z.P.; Wu, X.S.; Tan, W.S. Sr Content on the Structure and Magnetic Properties of $La_{1-x}Sr_xCoO_3$. *J. Alloys Compd.* **2009**, *474*, 81−85.

(43) Gunasekaran, R.A.; Pedarnig, J.D.; Dinescu, M. Structural, Electrical, and Surface Characteristics of $La_{0.5}Sr_{0.5}CoO_3$ Thin Films Prepared by Pulsed-Laser Deposition. *Appl. Phys. A* **1999**, *69*, 621−624.

(44) Bychkov, S.F.; Sokolov, A.G.; Popov, M.P.; Nemudry, A.P. Relation between Oxygen Stoichiometry and Thermodynamic Properties and the Electronic Structure of Nonstoichiometric perovskite $La_{0.6}Sr_{0.4}CoO_{3-\delta}$. *Phys. Chem. Chem. Phys.* **2016**, *18*, 29543−29548.

(45) Luo, G.P.; Wang, Y.S.; Chen, S.Y.; Heilman, A.K.; Chen, C.L.; Chu, C.W.; Liou, Y.; Ming, N.B. Electrical and Magnetic Properties of $La_{0.5}Sr_{0.5}CoO_3$ Thin Films. *Appl. Phys. Lett.* **2000**, *76*, 1908−1910.

(46) Li, M.; Wang, Z.L.; Fan, S.; Zhao, Q.T.; Xiong, G. Influences of Substrates and Substrate Temperatures on Characteristics of Epitaxial $La_{0.5}Sr_{0.5}CoO_3$ Thin Films. *Thin Solid Films* **1998**, *323*, 304−308.

(47) Fister, T.T.; Esbenshade, J.; Chen, X.; Long, B.R.; Shi, B.; Schlepütz, C.M.; Gewirth, A.A.; Bedzyk, M.J.; Fenter, P. Lithium Intercalation Behavior in Multilayer Silicon Electrodes. *Adv. Energy Mater*. **2014**, *4*, 1301494.

(48) Chan, P.W.; Wu, W.; Wong, K.H.; Tong, K.Y.; Cheung, J.T. Preparation and Characterization of Epitaxial Films and of an All a-Axis Oriented $YBa_2Cu_3O_{7-y}/La_{0:5}Sr_{0:5}CoO_3/YBa_2Cu_3O_{7-y}$ Heterostructure on (001) $LaAlO_3$ by Pulsed Laser Deposition. *J. Phys. D: Appl. Phys.* **1997**, *30*, 957−961.

(49) Wu, W.; Lu, F.; Wong, K.H.; Pang, G.K.H.; Choy, C.L.; Zhang, Y.H. Epitaxial and Highly Electrical Conductive $La_{0.5}Sr_{0.5}CoO_3$ Films Grown by Pulsed Laser Deposition in Vacuum. *J. Appl. Phys.* **2000***, 88,* 700−704.

(50) Filies, O.; Böling, O.; Grewer, K.; Lekki, J.; Lekka, M.; Stachura, Z.; Cleff, B. Surface Roughness of Thin Layers—a Comparison of XRR and SFM Measurements. *Appl. Surf. Sci.* **1999**, *141*, 357−365.

(51) Rougier, A.; Striebel, K.A.; Wen, S.J.; Cairns, E.J. Cyclic Voltammetry of Pulsed Laser Deposited $Li_xMn_2O_4$ Thin Films. *J. Electrochem. Soc.* **1998**, *145*, 2975−2980.

(52) Piszora, P.; Nowicki, W.; Darul, J.; Wolska, E. Synthesis and Characterization of the Lithium-Deficient Fe-substituted Li–Mn Oxide Spinel Phases. *Mater. Lett.* **2004**, *58*, 1321−1326.

(53) Mukai, K.; Sugiyama, J.; Kamazawa, K.; Ikedo, Y.; Andreica, D.; Amato, A. Magnetic Properties of the Chemically Delithiated $Li_xMn_2O_4$ with $0.07 \leq x \leq 1$. *J. Solid State Chem*. **2011**, *184*, 1096−1104.

(54) Kanno, R.; Kondo, A.; Yonemura, M.; Gover, R.; Kawamoto, Y.; Tabuchi, M.; Kamiyama, T.; Izumi, F.; Masquelier, C.; Rousse, G. The Relationships between Phases and Structures of Lithium Manganese Spinels. *J. Power Sources* **1999**, *81*, 542−546.

(55) Matthews, J.W.; Blakeslee, A.E. Defects in Epitaxial Multilayers: II. Dislocation Pile-ups, Threading Dislocations, Slip Lines and Cracks. *J. Cryst. Growth* **1975**, *29*, 273−280.

(56) Whall, T.E.; Parker, E.H.C. SiGe Heterostructures for FET Applications. *J. Phys. D: Appl. Phys*. **1998**, *31*, 1397−1416.

(57) Baskaran, A.; Smereka, P. Mechanisms of Stranski-Krastanov Growth. *J. Appl. Phys*. **2012**, *111*, 044321.

(58) Hull, R.; Gray, J.; Wu, C.C.; Atha, S.; Floro, J.A. Interaction between Surface Morphology and Misfit Dislocations as Strain Relaxation Modes in Lattice-Mismatched Heteroepitaxy. *J. Phys: Condens. Matter* **2002**, *14*, 12829−12841.

(59) Benedek, R.; Thackeray, M.M.; Low, J.; Bučko, T. Simulation of Aqueous Dissolution of Lithium Manganate Spinel from First Principles. *J. Phys. Chem. C* **2012**, *116*, 4050−4059.

(60) Reddy, M.V.; Pecquenard, B.; Vinatier, P.; Levasseur, A. Cyclic Voltammetry and Galvanostatic Cycling Characteristics of $LiNiVO_4$ Thin Films during Lithium Insertion and Re/De-insertion. *Electrochem. Commun.* **2007**, *9*, 409−415.

(61) Oh, M.Y.; Lee, J.J.; Zahoor, A.; Nahm, K.S. Enhanced Electrocatalytic Activity of Three-Dimensionally-Ordered Macroporous $La_{0.6}Sr_{0.4}CoO_{3-\delta}$ Perovskite Oxide for $Li–O_2$ Battery Application. *RSC Adv*. **2016**, *6*, 32212−32219.

(62) Yi, L. U.; Le, C. H. E. N.; Chunhua, L. U.; Yaru, N. I.; Zhongzi, X. U. Effects of Oxygen Defects on Structure and Properties of $Sm_{0.5}Sr_{0.5}CoO_{3-\delta}$ Annealed in Different Atmospheres. *J. Rare Earths* **2013**, *31*, 1183−1190.

(63) Gunasekaran, N.; Rajadurai, S.; Carberry, J.J.; Bakshi, N.; Alcock, C.B. Surface Characterization and Catalytic Properties of $La_{1-x}A_xMO_3$ Perovskite Oxides. Part II. Studies on $La_{1-x}Ba_xMnO_3$ ($0 \leqslant x \leqslant 0.2$) Oxides. Solid State Ionics **1995**, *81*, 243−249.

TOC graphic

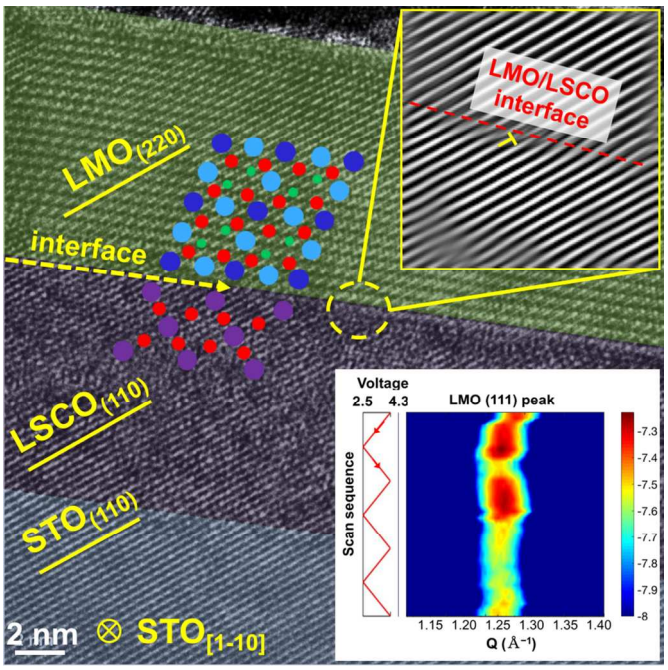
LMO/LSCO interface
LMO (220)
interface
LSCO (110)
STO (110)
2 nm ⊗ STO [1-10]
Voltage
2.5 4.3
LMO (111) peak
Scan sequence
-7.3
-7.4
-7.5
-7.6
-7.7
-7.8
-7.9
-8
1.15 1.20 1.25 1.30 1.35 1.40
Q (Å⁻¹)